Congenital Zika virus infection as a silent pathology with loss of neurogenic output in the fetal brain

Kristina M Adams Waldorf[1–4], Branden R Nelson[5,19], Jennifer E Stencel-Baerenwald[2,6,19], Colin Studholme[7,8,9,19], Raj P Kapur[10,11,19], Blair Armistead[3,12,19], Christie L Walker[1,19], Sean Merillat[12,19], Jay Vornhagen[3,12,19], Jennifer Tisoncik-Go[2,6,19], Audrey Baldessari[13], Michelle Coleman[7,12], Manjiri K Dighe[9], Dennis W W Shaw[9,14], Justin A Roby[2,6], Veronica Santana-Ufret[12], Erica Boldenow[7,12], Junwei Li[8], Xiaohu Gao[8], Michael A Davis[2,6], Jesica A Swanstrom[15], Kara Jensen[15], Douglas G Widman[15], Ralph S Baric[15,16], Joseph T Medwid[17], Kathryn A Hanley[17], Jason Ogle[13], G Michael Gough[13], Wonsok Lee[13], Chris English[13], W McIntyre Durning[13], Jeff Thiel[9], Chris Gatenby[9], Elyse C Dewey[2,6], Marian R Fairgrieve[2,6], Rebecca D Hodge[18], Richard F Grant[13], LaRene Kuller[13], William B Dobyns[5,7], Robert F Hevner[5], Michael Gale Jr[2,3,6] & Lakshmi Rajagopal[2,3,7,12]

Zika virus (ZIKV) is a flavivirus with teratogenic effects on fetal brain, but the spectrum of ZIKV-induced brain injury is unknown, particularly when ultrasound imaging is normal. In a pregnant pigtail macaque (*Macaca nemestrina*) model of ZIKV infection, we demonstrate that ZIKV-induced injury to fetal brain is substantial, even in the absence of microcephaly, and may be challenging to detect in a clinical setting. A common and subtle injury pattern was identified, including (i) periventricular T2-hyperintense foci and loss of fetal noncortical brain volume, (ii) injury to the ependymal epithelium with underlying gliosis and (iii) loss of late fetal neuronal progenitor cells in the subventricular zone (temporal cortex) and subgranular zone (dentate gyrus, hippocampus) with dysmorphic granule neuron patterning. Attenuation of fetal neurogenic output demonstrates potentially considerable teratogenic effects of congenital ZIKV infection even without microcephaly. Our findings suggest that all children exposed to ZIKV *in utero* should receive long-term monitoring for neurocognitive deficits, regardless of head size at birth.

A recent ZIKV epidemic in the Americas became a global public health emergency after an unexpected surge in prenatal and congenital microcephaly suggested that the virus was teratogenic in pregnancy. ZIKV is a flavivirus transmitted by the bite of *Aedes* mosquitoes. ZIKV is neurotropic and can target neural progenitor cells, astrocytes and neurons in all stages of development[1]. Infection typically induces an asymptomatic or mild infection characterized by fever, rash and arthralgia. The congenital ZIKV syndrome comprises a pattern of severe fetal brain injury, including microcephaly and ocular injury, associated with infection during pregnancy[2]. Counseling pregnant women with ZIKV infection is limited by a lack of understanding of the spectrum and prevalence of fetal injury[3]. Although the association between ZIKV and microcephaly is known, recent reports have supported a broad spectrum of injury, including eye abnormalities and development of postnatal microcephaly[4–8], in infants with a normal head circumference at birth. There is an urgent need for development of a pathophysiologically relevant animal model to support preclinical characterization of vaccines[9–14] and therapeutics[15,16]. We previously reported fetal brain injury in a pregnant pigtail macaque (*M. nemestrina*) subcutaneously infected with ZIKV[17]. Here we describe an expanded series of ZIKV infections in pregnant pigtail macaques, including the prior case report[17], wherein substantial loss of fetal neuronal progenitor cells accompanied a characteristic pattern of brain injury.

We inoculated ZIKV subcutaneously at five separate locations on the forearms (total inoculum, 5×10^7 plaque-forming units) of five healthy pregnant pigtail macaques, identified as ZIKA 1, 2, 3, 4 and 5 (**Supplementary Fig. 1** and **Supplementary Table 1**). A Cambodian ZIKV strain (F2213025; 2010) was inoculated at 119 d gestation (ZIKA 1 (ref. 17)) and 82 d gestation (ZIKA 2). For ZIKA 3–5, a Brazilian ZIKV strain (Fortaleza; 2015) was inoculated with *Aedes aegypti* salivary gland extract (SGE; ~4 glands per inoculum; shown to enhance flavivirus infection)[18,19] at 60–63 d gestation. ZIKA 3–5 also received a monoclonal dengue virus antibody (DENV-Ab; EDE2 B7, 1 mg intravenously)[20] prior to viral inoculation and at 3 weeks following inoculation to model antibody-dependent enhancement, which is thought to occur in some human cases owing to DENV-Ab (**Supplementary Fig. 2**)[21,22]. Control (CTRL) monkeys were inoculated with medium together with mosquito SGE and EDE2 B7 antibody (CTRL 2) or with medium alone (CTRL 1, 3). Prior to inoculation, all monkeys were seronegative for ZIKV and related flaviviruses (**Supplementary Table 2**). Monkeys were delivered via Cesarean section in the absence of labor within 1 month of their due date to enable collection of placental and fetal tissues before birth (~172 d gestation).

Three of the five ZIKA monkeys appeared healthy without evidence of fever, conjunctivitis or obstetrical complications of pregnancy (e.g., preterm labor). Seven days after inoculation, ZIKA 3 developed intermittent rectal bleeding. In ZIKA 5, a rash developed on the forearms 2 d after inoculation and resolved after 6 d (**Supplementary Fig. 3**). ZIKV IgG became detectable in the maternal sera of all ZIKA monkeys between 10–18 d after inoculation and in the amniotic fluid from four of the five ZIKA fetuses (**Supplementary Table 2**). ZIKV RNA was detected in the maternal sera of ZIKA monkeys only on day 2 and not in controls (**Supplementary Fig. 4a**). ZIKV RNA was also detected in brain and other organs from ZIKA 1 and 2 and their fetuses but not in controls or ZIKA monkeys with a longer latency between inoculation and delivery (**Supplementary Table 3**). ZIKV infectious isolates were recovered from the maternal plasma of the two monkeys with the highest viral load (ZIKA 4 and 5; **Supplementary Fig. 4b**).

No obvious fetal abnormalities were detected through weekly ultrasound with the exception of a periventricular echogenic lesion and ventriculomegaly in ZIKA 1, as previously described[17]. Over time, maternal ZIKV infection was associated with a growth deceleration, particularly in late gestation, in abdominal circumference and fetal biparietal diameter, which did not meet criteria for microcephaly (biparietal diameter <2 s.d. below the mean; **Supplementary Fig. 5**). Doppler assessment of the fetal middle cerebral artery revealed no differences in the resistance index, suggesting that fetal brain oxygenation was similar between the groups (mean, 0.7; both groups). Fetal brain magnetic resonance imaging (MRI) scans taken using a half-Fourier acquisition single-shot turbo spin-echo, T2-weighted (HASTE) pulse sequence were abnormal in four of the five fetuses (**Supplementary Fig. 1**). Periventricular–subcortical T2-hyperintense foci developed in the posterior brain in the fetuses of ZIKA 1–3 and 5 between 120–129 d gestation and were absent in the fetuses of controls (**Fig. 1a** and **Supplementary Figs. 6–11**). The brainstem and cerebellum appeared normal in all fetuses with the exception of a posterior fossa arachnoid cyst in ZIKA 1 (**Supplementary Fig. 12**). We controlled for natural variations in fetal brain size by analyzing the proportion that noncortical tissues (excluding cortical plate) contributed to overall fetal brain volume (**Fig. 1b** and **Supplementary Fig. 13**). The ratio of noncortical tissues to total brain volume was
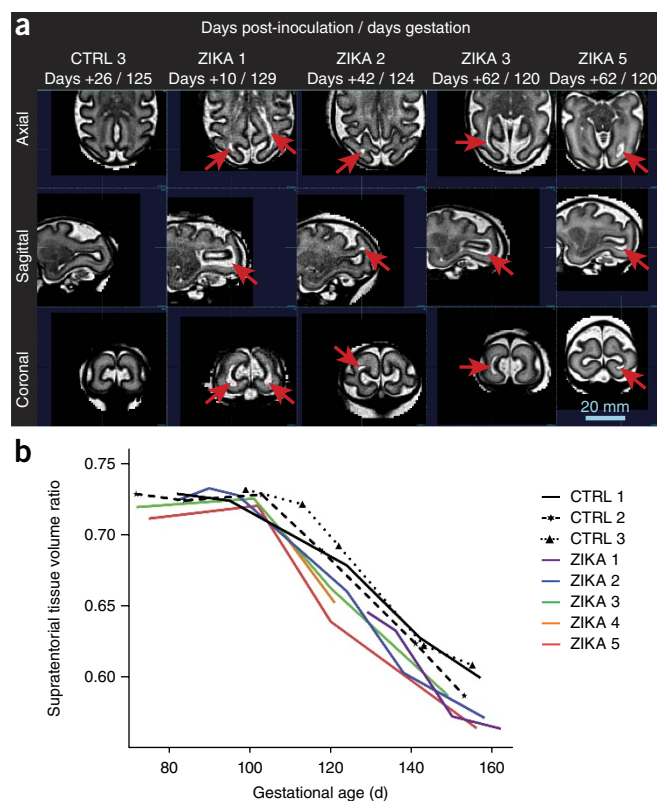
Figure 1 Fetal brain MRI imaging and volume analysis. (**a**) Serial fetal brain MRI images (HASTE) from fetuses of pigtail macaques inoculated with ZIKV or control medium showing differences in structure and volume. Four of five ZIKA fetuses demonstrated periventricular–subcortical T2-hyperintense foci (red arrows) in white matter of posterior brain between 120–129 d gestation; these were absent in control fetuses at the same developmental age. Images were segmented to obtain specific brain volumes for each region (e.g., white matter, cortical gray matter; **Supplementary Fig. 13**). (**b**) A plot showing the change in the supratentorial (fetal brain) tissue volume ratio in the latter half of pregnancy; this ratio estimates the contribution of noncortical tissues (excluding cortical plate) to the overall volume of the brain (excluding cerebellum).

similar among ZIKA fetuses and controls until ~100 d gestation, which was when the relative proportions of noncortical tissues to overall brain volume began to diverge, leading to a significantly smaller ratio in ZIKA fetuses at delivery ($P = 0.01$, unpaired two-tailed Welch's t-test with unequal variances; **Fig. 1b**).

We previously described neuropathology in the fetus of ZIKA 1, which demonstrated ependymal loss, fusion of ventricular surfaces, periventricular gliosis, white matter gliosis and axonal spheroids (axonal injury)[17]. A consistent pattern of neuropathology was identified in ZIKA 2–4 fetuses, which showed a spectrum of severity in these features, and was absent in controls; the most consistent finding was ependymal injury in the posterior lateral ventricles. Ependymal loss, interruption of the lumen, fusion of denuded ventricular surfaces and/or glial fibrillary acidic protein (GFAP)-immunoreactive gliosis in white matter beneath the ventricle surface were most prominent in the fetuses of ZIKA 1 and 2, and there were similar but milder changes in the ZIKA 3 and 4 fetuses (**Fig. 2** and **Supplementary Table 4**). There was no substantial neuropathology in the ZIKA 5 fetus; notably, and in contrast to the other ZIKA fetuses, natural killer

(NK) cell populations in the placenta and maternal blood of ZIKA 5 were similar to controls (**Supplementary Fig. 14**). No distinct pathologic abnormalities were seen in other fetal or maternal organs with the exception of minimal maternal myocardial fibrosis in ZIKA 4. Placental histopathology revealed only mild deciduitis, which was also present in some controls (**Supplementary Fig. 15**).

ZIKV infects and kills neural stem cells (NSCs), including early neuroepithelial progenitors, radial glia and intermediate progenitor cells (IPs)[23,24]. As we ended the study near the natural due date, we hypothesized that remaining 'late' neurogenic populations in the subventricular zone (SVZ) of the temporal cortex and the subgranular zone (SGZ) of the dentate gyrus in the fetal hippocampus were affected by congenital ZIKV exposure (**Fig. 3a–c**)[25–28]. Although SVZ and SGZ NSCs are actively neurogenic and express similar markers, each population generates different types of neurons[29] and may be differentially affected by ZIKV[30] owing to lateral ventricle proximity, differences in regional vasculature and sensitivity to inflammatory signals. We immunolabeled sections of fetal brain for the proliferative marker Ki67 (**Fig. 3d–g**) and found a significant reduction in Ki67$^+$ cells in the SVZ of ZIKA fetuses relative to controls ($P = 0.03$, unpaired two-tailed Welch's t-test with unequal variances), whereas there was no such difference in the SGZ (**Fig. 3h** and **Supplementary Fig. 16**). We also immunolabeled adjacent sections for SRY (sex determining region Y)-box 2 (SOX2) and T-box brain protein 2 (TBR2; also known as EOMES) proteins (**Fig. 4a–c** and **Supplementary Fig. 16**), which mark quiescent and active NSCs and IPs, respectively[31,32]. Congenital ZIKV exposure was associated with a trend towards reduction in fetal SOX2$^+$ cells in the SVZ ($P = 0.06$, unpaired two-tailed Welch's t-test with unequal variances; **Fig. 4d**); in the SGZ niche, SOX2$^+$ NSCs appeared disorganized. TBR2$^+$ IPs in ZIKA fetuses were significantly reduced in the SGZ relative to controls ($P = 0.006$, unpaired two-tailed Welch's t-test with unequal variances; **Fig. 4e–h** and **Supplementary Fig. 17**). Moreover, SOX2–TBR2–doublecortin (DCX) triple immunolabeling of adjacent sections revealed that SOX2$^+$ NSC disorganization and loss of TBR2$^+$ IPs in the SGZ niche were accompanied by dysmorphia in the DCX$^+$ maturing granule neuron (GN) neural circuitry (**Fig. 4f–h** and **Supplementary Fig. 18**). Flow cytometry analysis of cells isolated from cortical white matter tracts also revealed a significant increase in astrocytes with congenital ZIKV exposure, indicating a gliotic response to nervous system injury ($P = 0.02$, unpaired two-tailed Welch's t-test with unequal variances; **Supplementary Fig. 19**).

An enduring obstetric challenge of the ZIKV epidemic is antenatal identification of the spectrum of ZIKV-associated fetal brain injury not captured by the definition of the congenital ZIKV syndrome. Our study reveals that ZIKV exposure can cause a spectrum of subtle fetal brain injuries in the absence of overt microcephaly, including loss of late fetal NSCs that normally persist into adult life, perturbations to neuron patterning and astrocyte gliosis. Within a highly relevant maternal–fetal transmission model of ZIKV infection, we identified a characteristic profile of fetal brain injury that is exceedingly difficult to clinically detect even with the aid of serial ultrasound and MRI. A deceleration in growth of the biparietal diameter and abdominal circumference may not be considered clinically abnormal, especially if the fetus is constitutionally large or ZIKV infection occurs late in gestation. T2-hyperintense foci were detected by MRI, but only transiently, and this imaging modality is not widely available. Our study highlights the inability of standard prenatal diagnostic tools to detect silent pathology in the fetal brain associated with congenital ZIKV infection in the absence of microcephaly.
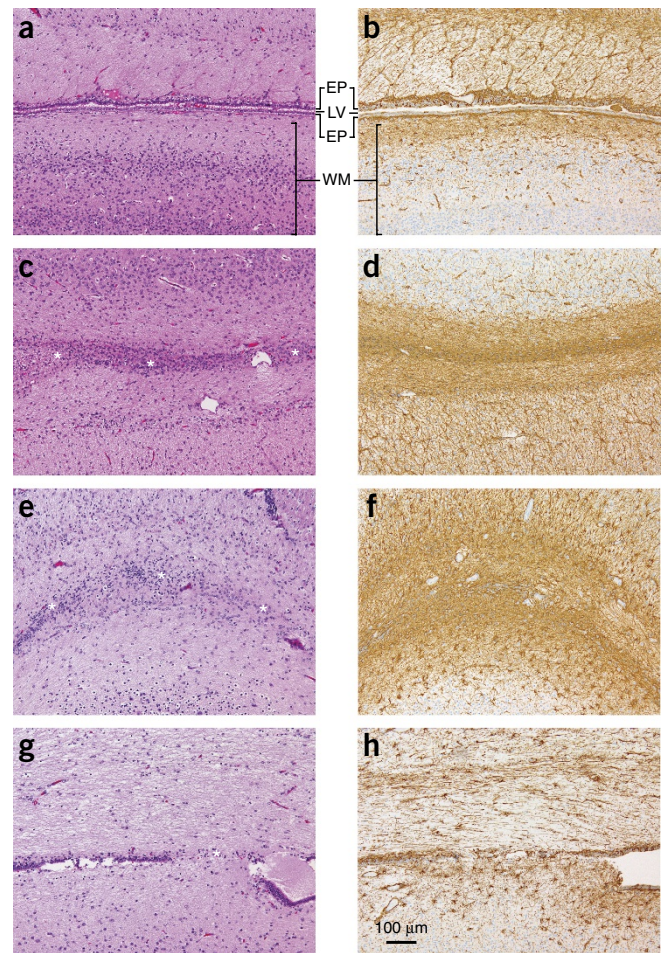
Figure 2 Neuropathology of the fetal brain demonstrating ZIKV-associated ependymal fusion and periventricular gliosis. (**a–h**) Microscopic images of H&E-stained sections of the lateral ventricle (LV) with ependymal epithelium (EP) are shown for a control (**a**) and for ZIKA 1, 2 and 4 fetuses (**c**, **e** and **g**, respectively). Immunostaining for GFAP is also shown in the same control (**b**) and the respective ZIKV fetuses (**d**, **f** and **h**) in an adjacent section. Asterisks indicate zones of ependymal fusion. GFAP immunostaining demonstrates periventricular gliosis (brown staining) in regions surrounding ependymal fusion. WM, white matter.

Our new finding that ZIKV attenuates late fetal neurogenesis is concerning because there may be long-term neurocognitive effects in fetuses that did not meet the criteria for microcephaly at birth. Neurogenesis normally persists in the human hippocampus through at least adolescence[33] and is important for learning[29] and memory[29]. Attenuation of NSC and IP populations may predispose not only to microcephaly but also to the long-term development of Alzheimer's disease[34], schizophrenia[35] and depression[36]. The loss of adult NSCs due to ZIKV infection has been reported in a highly immunocompromised nonpregnant mouse (lacking interferon regulatory factor 3 (IRF3), IRF5 and IRF7)[37]. Our findings now confirm that NSC populations, which typically persist through at least adolescence, are impacted in the fetus of an immunocompetent and pathophysiologically relevant nonhuman primate model. If altered neurogenesis occurs in human children and adolescents infected with ZIKV after birth, similar to our findings in fetal nonhuman primates, a risk for the early onset of neurocognitive and psychiatric conditions could extend beyond infection *in utero*. It is also possible that quiescent
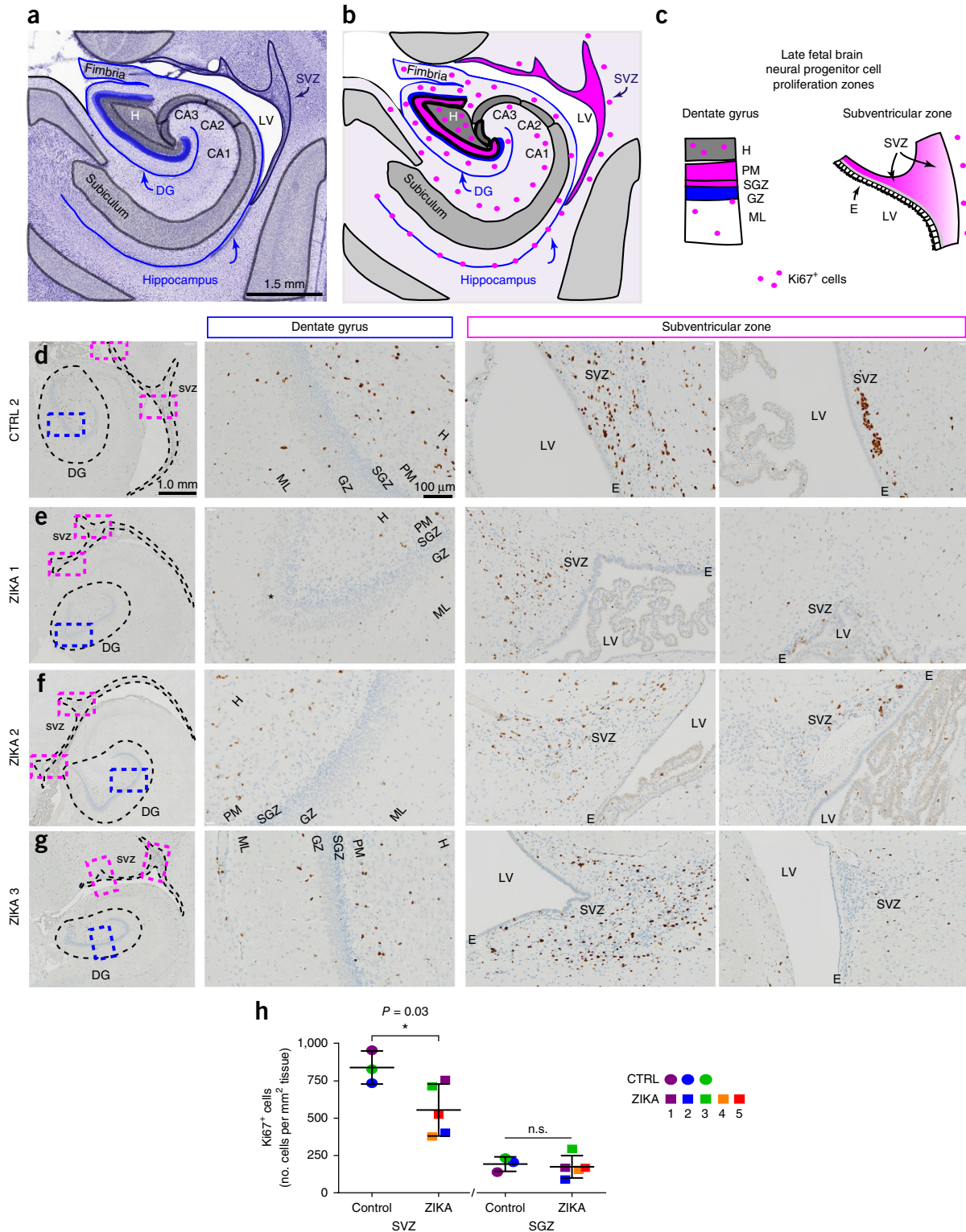
Figure 3 NSC proliferation is reduced in late fetal neurogenic zones. (**a**) A schematic of the fetal temporal cortical SVZ and hippocampus for a rhesus macaque neonate (0 months) with a Nissl-stained section. The schematic is based on the National Institutes of Health (NIH) Blueprint Nonhuman Primate Atlas (http://www.blueprintnhpatlas.org/). (**b,c**) Diagrams indicating the locations of proliferating Ki67^{+} NSCs (pink dots and pink regions) in neurogenic niches of the tissue (**b**) and specific regions of the SVZ and hippocampus (**c**). CA, cornu ammonis; DG, dentate gyrus; E, ependymal; GZ, granule zone; H, hilus; ML, molecular layer; PM, polymorphic layer. (**d–g**) Ki67^{+} cells in the dentate gyrus and the SVZ, key regions of neurogenesis, are shown for a control (**d**) and ZIKA fetuses (**e–g**), with higher-power views of the dentate gyrus (blue box) and SVZ regions (pink box) shown at the right. (**h**) Quantification of Ki67^{+} cells showing a significant decrease in proliferation in the SVZ of ZIKV-infected fetuses as compared to the SGZ and controls. Data are shown as means ± s.d. of Ki67^{+} cell counts per mm². Statistical analysis was performed with an unpaired two-tailed Welch's t-test with unequal variances. *$P < 0.05$; n.s., nonsignificant.

NSCs may become activated to repair neural circuitry following less severe ZIKV-induced injury.

The strength of our study lies in the first *in vivo* molecular characterization, to our knowledge, of the effects of maternal ZIKV infection on the fetal brain demonstrating (i) deficient fetal neuronal progenitor cell populations concomitant with loss of noncortical volume in fetal brain, (ii) perturbations in neuron maturation and patterning in the hippocampus and (iii) increased astrocyte gliosis. Less white matter gliosis in ZIKA 3–5 fetuses (inoculation, ~60 d gestation) than in ZIKA 1 and 2 fetuses (inoculation, 82–119 d gestation) may reflect

Figure 4 Attenuated neurogenesis in late fetal neurogenic zones accompanied by granule neuron dysmorphia in the dentate gyrus after maternal ZIKV infection. (**a**–**c**) Adjacent sections labeled for SOX2$^+$ NSCs (left) and TBR2$^+$ IPs (right) by immunohistochemistry (brown). Congenital ZIKV exposure results in reduction of fetal SOX2$^+$ NSCs in the SVZ and disorganization in the SGZ. Asterisks indicate disordered NSCs in the SGZ neurogenic niche. Arrows indicate a loss of continuity in the granule zone. (**d**,**e**) Plots showing the number of SOX2$^+$ and TBR2$^+$ NSCs in the SVZ (**d**) and SGZ (**e**) from the immunohistochemistry in **a**–**c**. (**f**–**h**) Confocal microscopy images showing NSCs (SOX2$^+$, red), IPs (TBR2$^+$, green) and immature granule neurons (DCX$^+$, white; DAPI nuclei, blue) in adjacent sections, revealing disordered NSCs in the SGZ niche, loss of neurogenic output (TBR2$^+$ IPs) and dysmorphic granule neurons with congenital ZIKV exposure. Statistical analysis was performed with an unpaired two-tailed Welch's *t*-test with unequal variances. Data are shown as means ± s.d. of either SOX2$^+$ or TBR2$^+$ cell counts per mm^2. **$P < 0.01$.

the limited capacity for a gliotic response of the early fetal brain rather than differences in viral strain or lack of potentiation by *A. aegypti* salivary gland proteins or antibody-dependent enhancement[38]. The sample size precludes drawing conclusions as to slight variations in study design, which reflected attempts to observe a more severe phenotype with inoculation earlier in pregnancy coupled with a Brazilian ZIKV strain and DENV-Ab to model antibody-dependent enhancement[20]. Despite variations in study design (e.g., viral strain), the effect of maternal ZIKV infection on fetal NSC loss was fairly consistent in all ZIKV monkeys; notably, inoculation with SGE and DENV-Ab alone was not associated with fetal brain injury in CTRL 2. Although antibody-dependent enhancement was not demonstrated in a study of nonpregnant nonhuman primates[39], this question should be evaluated in pregnancy and the developing fetus. A recent study associating DENV-Ab titer with severe dengue disease in a large pediatric cohort provides important evidence for enhancement associated with antibody titer, which is challenging to model experimentally[40].

Our findings underscore the formidable obstetric challenge of diagnosing ZIKV-associated fetal brain injury, as a loss in fetal brain volume may be subtle and normal ultrasound imaging of the fetal brain does not correlate with the absence of fetal brain injury. Attenuation and/or loss of NSCs not only elevates concern for long-term effects of congenital ZIKV exposure for neonates regardless of head size at birth but also for children and young adults who acquire ZIKV after birth. Additional research is needed to determine whether ZIKV infection *in utero* or in childhood is associated with an elevated risk for neurocognitive and psychiatric disorders.

METHODS

Methods, including statements of data availability and any associated accession codes and references, are available in the online version of the paper.

Note: Any Supplementary Information and Source Data files are available in the online version of the paper.

AUTHOR CONTRIBUTIONS
K.M.A.W., B.R.N., J.E.S.-B., R.P.K., C.S., R.S.B., D.G.W., M.G. and L.R. designed the study. K.M.A.W., B.R.N., J.E.S.-B., R.P.K., C.S., R.P.K., B.A., S.M., J.T.-G., A.B., M.C., J.A.R., J.V., V.S.-U., E.B., J.A.S., J.L., M.A.D., K.J., D.G.W., J.T.M., K.A.H., J.O., G.M.G., W.L., C.E., W.M.D., C.G., E.C.D., M.R.F., L.K. and L.R. performed the experiments. K.M.A.W., B.R.N., J.E.S.-B., C.S., R.P.K., B.A., C.L.W., S.M., J.T.-G., A.B., M.K.D., D.W.W.S., J.A.R., J.V., J.L., X.G., M.A.D., J.A.S., K.J., R.S.B., R.D.H., R.F.G., W.B.D., R.H., L.R., R.F.H., M.G. and L.R. analyzed the data. K.M.A.W., B.R.N., J.E.S.-B., C.S., R.P.K., B.A., C.L.W., A.B., W.B.D., M.G. and L.R. drafted the manuscript. All authors reviewed the final draft of the manuscript.

1. van den Pol, A.N., Mao, G., Yang, Y., Ornaghi, S. & Davis, J.N. Zika virus targeting in the developing brain. *J. Neurosci.* **37**, 2161–2175 (2017).
2. Moore, C.A. *et al.* Characterizing the pattern of anomalies in congenital Zika syndrome for pediatric clinicians. *JAMA Pediatr.* **171**, 288–295 (2016).
3. Maurice, J. The Zika virus public health emergency: 6 months on. *Lancet* **388**, 449–450 (2016).
4. França, G.V.A. *et al.* Congenital Zika virus syndrome in Brazil: a case series of the first 1501 livebirths with complete investigation. *Lancet* **388**, 891–897 (2016).
5. Mlakar, J. *et al.* Zika virus associated with microcephaly. *N. Engl. J. Med.* **374**, 951–958 (2016).
6. Driggers, R.W. *et al.* Zika virus infection with prolonged maternal viremia and fetal brain abnormalities. *N. Engl. J. Med.* **374**, 2142–2151 (2016).
7. Moura da Silva, A.A. *et al.* Early growth and neurologic outcomes of infants with probable congenital Zika virus syndrome. *Emerg. Infect. Dis.* **22**, 1953–1956 (2016).
8. Del Campo, M. *et al.* The phenotypic spectrum of congenital Zika syndrome. *Am. J. Med. Genet. A* **173**, 841–857 (2017).
9. Richner, J.M. *et al.* Modified mRNA vaccines protect against Zika virus infection. *Cell* **168**, 1114–1125 (2017).
10. Betancourt, D., de Queiroz, N.M., Xia, T., Ahn, J. & Barber, G.N. Cutting edge: innate immune augmenting vesicular stomatitis virus expressing Zika virus proteins confers protective immunity. *J. Immunol.* **198**, 3023–3028 (2017).
11. Chahal, J.S. *et al.* An RNA nanoparticle vaccine against Zika virus elicits antibody and CD8+ T cell responses in a mouse model. *Sci. Rep.* **7**, 252 (2017).
12. Sumathy, K. *et al.* Protective efficacy of Zika vaccine in AG129 mouse model. *Sci. Rep.* **7**, 46375 (2017).
13. Shan, C. *et al.* A live-attenuated Zika virus vaccine candidate induces sterilizing immunity in mouse models. *Nat. Med.* **23**, 763–767 (2017).
14. Yang, Y. *et al.* A cDNA clone-launched platform for high-yield production of inactivated Zika vaccine. *EBioMedicine* **17**, 145–156 (2017).
15. Sapparapu, G. *et al.* Neutralizing human antibodies prevent Zika virus replication and fetal disease in mice. *Nature* **540**, 443–447 (2016).
16. Ireton, R.C. & Gale, M. Jr. RIG-I like receptors in antiviral immunity and therapeutic applications. *Viruses* **3**, 906–919 (2011).
17. Adams Waldorf, K.M. *et al.* Fetal brain lesions after subcutaneous inoculation of Zika virus in a pregnant nonhuman primate. *Nat. Med.* **22**, 1256–1259 (2016).
18. Styer, L.M. *et al.* Mosquito saliva causes enhancement of West Nile virus infection in mice. *J. Virol.* **85**, 1517–1527 (2011).
19. Conway, M.J. *et al.* Mosquito saliva serine protease enhances dissemination of dengue virus into the mammalian host. *J. Virol.* **88**, 164–175 (2014).
20. Swanstrom, J.A. *et al.* Dengue virus envelope dimer epitope monoclonal antibodies isolated from dengue patients are protective against Zika virus. *MBio* **7**, e01123–16 (2016).
21. Dejnirattisai, W. *et al.* Dengue virus sero-cross-reactivity drives antibody-dependent enhancement of infection with Zika virus. *Nat. Immunol.* **17**, 1102–1108 (2016).
22. Paul, L.M. *et al.* Dengue virus antibodies enhance Zika virus infection. *Clin. Transl. Immunology* **5**, e117 (2016).
23. Lin, M.Y. *et al.* Zika virus infects intermediate progenitor cells and post-mitotic committed neurons in human fetal brain tissues. *Sci. Rep.* **7**, 14883 (2017).
24. Onorati, M. *et al.* Zika virus disrupts phospho-TBK1 localization and mitosis in human neuroepithelial stem cells and radial glia. *Cell Rep.* **16**, 2576–2592 (2016).
25. Smart, I.H., Dehay, C., Giroud, P., Berland, M. & Kennedy, H. Unique morphological features of the proliferative zones and postmitotic compartments of the neural epithelium giving rise to striate and extrastriate cortex in the monkey. *Cereb. Cortex* **12**, 37–53 (2002).
26. Bakken, T.E. *et al.* A comprehensive transcriptional map of primate brain development. *Nature* **535**, 367–375 (2016).
27. Miller, J.A. *et al.* Conserved molecular signatures of neurogenesis in the hippocampal subgranular zone of rodents and primates. *Development* **140**, 4633–4644 (2013).
28. Alvarez-Buylla, A. & Lim, D.A. For the long run: maintaining germinal niches in the adult brain. *Neuron* **41**, 683–686 (2004).
29. Gonçalves, J.T., Schafer, S.T. & Gage, F.H. Adult neurogenesis in the hippocampus: from stem cells to behavior. *Cell* **167**, 897–914 (2016).
30. McGrath, E.L. *et al.* Differential responses of human fetal brain neural stem cells to Zika virus infection. *Stem Cell Rep.* **8**, 715–727 (2017).

31. Hodge, R.D. *et al.* Tbr2 expression in Cajal-Retzius cells and intermediate neuronal progenitors is required for morphogenesis of the dentate gyrus. *J. Neurosci.* **33**, 4165–4180 (2013).
32. Hodge, R.D. *et al.* Tbr2 is essential for hippocampal lineage progression from neural stem cells to intermediate progenitors and neurons. *J. Neurosci.* **32**, 6275–6287 (2012).
33. Spalding, K.L. *et al.* Dynamics of hippocampal neurogenesis in adult humans. *Cell* **153**, 1219–1227 (2013).
34. Mu, Y. & Gage, F.H. Adult hippocampal neurogenesis and its role in Alzheimer's disease. *Mol. Neurodegener.* **6**, 85 (2011).
35. Duan, X. *et al.* Disrupted-In-Schizophrenia 1 regulates integration of newly generated neurons in the adult brain. *Cell* **130**, 1146–1158 (2007).
36. Jacobs, B.L., van Praag, H. & Gage, F.H. Adult brain neurogenesis and psychiatry: a novel theory of depression. *Mol. Psychiatry* **5**, 262–269 (2000).
37. Li, H. *et al.* Zika virus infects neural progenitors in the adult mouse brain and alters proliferation. *Cell Stem Cell* **19**, 593–598 (2016).
38. Rice, D. & Barone, S. Jr. Critical periods of vulnerability for the developing nervous system: evidence from humans and animal models. *Environ. Health Perspect.* **108** (Suppl. 3), 511–533 (2000).
39. McCracken, M.K. *et al.* Impact of prior flavivirus immunity on Zika virus infection in rhesus macaques. *PLoS Pathog.* **13**, e1006487 (2017).
40. Katzelnick, L.C. *et al.* Antibody-dependent enhancement of severe dengue disease in humans. *Science* **358**, 929–932 (2017).

ONLINE METHODS

Study design. The nonhuman primate experiments were carried out in strict accordance with the recommendations in the Guide for the Care and Use of Laboratory Animals of the National Research Council and the Weatherall report, "The use of non-human primates in research." The Institutional Animal Care and Use Committee (IACUC) of the University of Washington (UW) approved the study (permit number, 4165-02). Cesarean section was performed at least 10 d before the natural due date (~172 d gestation) to enable fetal and dam necropsy. We based the ZIKV inoculum dose on the feeding behavior of the ZIKV mosquito vector, *A. aegypti* (yellow fever mosquito), which deposits virus multiple times during skin probing prior to accessing a capillary for acquisition of the bloodmeal[41]. Five healthy pregnant pigtail macaques (*M. nemestrina*) received ZIKV (ZIKA 1–5) and three monkeys served as controls (CTRL 1–3) (**Supplementary Fig. 1** and **Supplementary Table 1**). In early pregnancy, CTRL 3 had a subchorionic placental hemorrhage with vaginal bleeding (confirmed by ultrasound) that self-resolved; this monkey was included in the study after her pregnancy stabilized and she had no bleeding for more than 1 month. Dual necropsy was performed earlier than planned for ZIKA 4 (~142 d gestation) after an anesthetic reaction resulted in the unexpected death of the dam.

Definition of fever in pigtail macaque. The definition of fever in pigtail macaque is not standardized. A range of rectal temperatures from 36.6–40.1 °C (average, 38.8 °C)[42] has been reported in sedated rhesus and cynomolgus macaques (*Macaca mulatta* and *Macaca fascicularis*, respectively), which are close relatives to the pigtail macaque. Individual variation is thought to relate to excitement prior to sedation and lowering of body temperature during sedation. The highest maternal rectal temperature recorded in the study was 38.6 °C (101.5 °F), which was not thought to represent a fever.

Mosquito salivary gland extracts. The New Mexico State University IACUC approved the procedures associated with obtaining mosquito salivary glands (permit number, 2015-003). *A. aegypti* (Rockefeller strain) mosquitoes were maintained as described[43]. Larvae were reared at 26.5 °C, 70% relative humidity, 16 h light–8 h dark cycle on a diet of cat food (Special Kitty, Walmart, USA); emerged adults were maintained on 20% sucrose *ad libitum*. Salivary glands dissected on ice from adults at 3 d of age were placed in a drop of PBS and stored at −80 °C. For homogenization, glands were aspirated >25 times using a syringe with a 23-gauge needle and 10 μl PBS per gland; samples were centrifuged at 14,000 r.p.m. for 10 min at 4 °C and stored at −80 °C.

Dengue virus antibody. A monoclonal antibody to a DENV envelope dimer-dependent epitope (EDE2 B7, IgG1 isotype) was synthetically generated by Lake Pharma from a published sequence, which is available upon request.

Ultrasound in nonhuman primates. Pregnancy dating was determined through measurement of the crown rump length in early pregnancy (~40–55 d gestation). Ultrasound was performed weekly, starting with ZIKV or control medium inoculation, for the duration of the study to confirm fetal viability, to survey fetal brain structure and to perform standard fetal ultrasound biometric measures, which were compared with published standards in pigtail macaques[44]. A GE Vivid i (GE Medical) machine was used for the first ultrasound and subsequent measurements were performed on the Philips HD11xe machine (Philips Healthcare). A curvilinear C9–4 MHz transducer was used to image the fetus. At least three measurements of the head circumference, abdominal circumference, biparietal diameter and femur length were acquired, and the average was calculated. Additionally, at least three ventricular measurements in the dependent ventricle, transverse cerebellar diameter and placental thickness were acquired, and the averages were calculated. At least two cine clips were acquired through the head (axial and coronal orientation), chest and abdomen (axial and sagittal orientation). Doppler ultrasound of the middle cerebral artery was performed to evaluate flow through the brain. Amniotic fluid index was calculated through measuring size of the fluid pockets in the four quadrants. Fetal biometry was compared to known standards for the pigtail macaque[44]. A board-certified radiologist (M.K.D.) with 13 years of experience in obstetric ultrasound reviewed the imaging. If a particular measurement or image was considered inadequate, this was excluded from the analysis.

Magnetic resonance imaging in nonhuman primates. MRI was performed using a Philips Achieva 3T scanner. A six-channel human cardiac RF coil was used for the early studies, and an eight-channel human knee coil was used for the later studies once it was determined that pregnant monkeys near term could fit in the knee coil. Anesthesia was induced using 5–20 mg ketamine per kg body weight and maintained using no higher than a 3% sevoflurane–oxygen mixture during the imaging. A three-plane localizer using a balanced Fast Field Echo (FFE) imaging sequence was used to determine fetal head position. A 2D single-shot, half-Fourier turbo spin echo multislice sequence (HASTE) was used to acquire T2-weighted images with the following parameters: TR/TE (repetition time/echo time) = 2,200/160 ms; SENSE acceleration factor = 2; TSE (turbospin echo) factor = 100; along with fat suppression and fold-over artifact suppression. Multiple contiguous 2D image stacks, with in-plane resolutions of 0.5×0.5 mm and thicknesses of 2 mm, were acquired along the axial, sagittal and coronal axes of the fetal brain to facilitate the reconstruction of a 3D volume with isotropic spatial resolution. Each 2-mm-thick plane orientation was repeated 6 times to provide high signal to noise in the final combined 3D reconstruction. MRI images were reviewed by a pediatric neuroradiologist (D.W.W.S.).

The first step to generate a single high-resolution 3D T2-weighted (T2W) image volume for quantitative analysis of tissue brain volume and surface anatomy was to import all multislice T2W image stacks with the SLIMMER slice motion correction tool[45] in Rview software (http://rview.colin-studholme.net, version 9.077.155BQT running under Ubuntu release 14). This step allowed for initial volume-based alignment to correct for gross drift of fetal head between slice stacks and to define a standardized orientation of fetal head anatomy. Between-slice motion occurring due to maternal breathing and fetal head drift was estimated using slice intersection motion correction[46]. Differences in signal intensity arising from drift of the fetal head with respect to the imaging coils during scanning and intensity variations due to spin history arising from motion between excitation and readout of each individual slice were corrected using slice intersection bias correction. Then, all slices were combined through an iterative deconvolution-based super-resolution 3D scattered data reconstruction technique using robust Huber-norm outlier rejection of any residual within-slice motion artifacts[47]. The final deconvolved isotropic spatial sampling resolutions of each image were selected to match the in-plane resolution of each slice (0.5 mm).

As no age-specific atlas is available for this species over the gestational period, we first manually traced tissues in selected MRI scans of the healthy reference fetuses so that we had a set of reference templates covering the full gestational age range in the study. This was achieved using an initial approximate automated intensity-based segmentation that was extensively edited using the Rview segmentation tool (http://rview.colin-studholme.net, version 9.077.155BQT running under Ubuntu release 14) to divide the tissues further into cortical and deep gray matter, white matter, cerebellum, sulcal cerebrospinal fluid (CSF) and ventricular CSF. These manually delineated reference images providing an example image of tissues at different gestational ages were then used as age-specific tissue templates for automated segmentation of each of the additional MRI scans of controls and ZIKV-infected fetuses. For each new scan, the nearest age-matched manually delineated template was used as a reference template for automated expectation–maximization-based segmentation[48]. Each automated segmentation was manually checked and edited to remove any residual cortical or subcortical tissue segmentation errors and to correct labeling of abnormal T2-hyperintense foci that were not present in the normal fetal template data. Regions of age-abnormal fluid representing abnormal posterior ventricular CSF regions and any surrounding disconnected regions of high T2-weighted signal were separately labeled as abnormal fluid volume. From these labeled images, we calculated the total supratentorial cortical gray matter, white matter and deep gray matter, the total cerebellum volume and the abnormal fluid volume in cubic centimeters.

Bacterial cultures. Bacterial cultures were performed to exclude microbial infection. Amniotic fluid collected at necropsy was plated on Tryptic Soy Agar (TSA) plates and incubated for 48 h at 37 °C in 5% CO_2. Swabs of maternal and

fetal meninges, lungs and chorioamniotic membranes were streaked on TSA plates and incubated for 48 h at 37 °C in 5% CO_2. No bacteria were cultured from any sample.

Serology for WNV, CHIKV, DENV and ZIKV in nonhuman primates. We used viral-specific ELISA assays for ZIKV, WNV, CHIKV and DENV IgG to test ultraviolet-inactivated serum according to the manufacturer's (Xpress Biosystems) instructions. Diluted plasma samples were added to the wells of the ELISA plate coated with viral antigens and incubated at 37 °C for 45 min. Wells were washed five times and peroxidase conjugate was added to each well and incubated for 45 min at 37 °C. Following incubation, the plate was washed five times followed by the addition of 2,2-azino-bis(3-ethylbenzothiazoline-6-sulphonic acid)-peroxidase substrate to each well. The plate was incubated at room temperature for 30 min, and the absorbance of the colorimetric reaction in each well was read within 15 min on a plate reader at 405 nm.

Neuropathology, immunohistochemistry and quantitative analyses. The Seattle Children's Hospital Research Laboratory Service Core performed immunohistochemistry for GFAP, TBR2, SOX2 and Ki67 on formalin-fixed paraffin-embedded sections of cerebral cortex or hippocampus from the ZIKV-exposed monkeys and controls. Immunostaining was performed with an automated immunostainer (Ventana) using the reagents and dilutions shown in **Supplementary Table 5**. Appropriate peroxidase-conjugated secondary antibodies and diaminobenzidine-based reaction product were used to visualize sites of immunoreactivity. All sections were blinded to case or control identity for quantitative analyses. Coded sections were imaged using an Olympus VS120 Slide Scanner. Temporal cortical SVZ and hippocampal dentate gyrus SGZ regions were defined using anatomical and methylene blue–counterstained cellular landmarks based on the available reference NIH Blueprint Nonhuman Primate Atlas (http://www.blueprintnhpatlas.org, rhesus macaque neonate 0 months). The SGZ included both the cell-dense SGZ and ~125 µm into the underlying polymorphic layer. Immunoreactive cells were automatically segmented using hue, saturation and value (HSV) thresholding. All identified cells were manually checked to correct for multiplicity and the number of positive single cells was determined per area (mm^2) using Olympus VS-Desktop software. Blinded cell counts were independently decoded and statistically analyzed (described below).

Cell lines and virus. Vero cells were obtained from the World Health Organization, and C6/36 *Aedes albopictus* cells were cultured in DMEM (Cellgro) supplemented with 10% FBS (HyClone), 2 mM L-glutamine, 1 mM sodium pyruvate, 100 U/ml of penicillin, 100 µg/ml of streptomycin and 1× nonessential amino acids (Sigma). The World Reference Center of Emerging Viruses and Arboviruses provided the ZIKV strain isolated in Cambodia (FSS13025, 2010; GenBank accession number: KU955593), and M. Diamond (Washington University) provided the ZIKV strain from Brazil (Fortaleza, 2015; GenBank accession number: KX811222.1). Working stocks were obtained through plaque-purifying virus amplified in either Vero (Cambodia strain) or C6/36 (Brazil strain) cells. Virus was adsorbed to cells in DMEM supplemented to contain 1% FBS at 37 °C for 2 h. The inoculum was removed and virus was propagated in medium supplemented to contain 5% FBS, 2 mM L-glutamine, 1 mM sodium pyruvate, 100 U/ml penicillin, 100 µg/ml streptomycin, 20 mM HEPES and 1× nonessential amino acids (Sigma). Supernatants were collected and spun at 2,000 r.p.m. at 4 °C for 10 min and were frozen in aliquots at −80 °C. All cell lines used lacked mycoplasma.

Measurement of ZIKV RNA load. Viral RNA load was assessed in tissues from the dam, fetus and placenta using a ZIKV-specific RT–qPCR assay. Fetal and maternal organs were immersed in RNAlater immediately upon dissection and were then weighed and homogenized in RLT solution (Qiagen) using a bead-beater apparatus (Precellys). RNA was extracted from tissues using the RNeasy kit (Qiagen) and from sera using the ZR Viral RNA extraction kit (Zymo Research). From tissues, 400 ng of total RNA was used to generate cDNA using the iScript select cDNA synthesis kit (Bio-Rad), according to the manufacturer's protocols, for gene-specific primers. Viral RNA was quantified using the TaqMan Universal Master Mix (Applied Biosystems) and an Applied

Biosystems 7300 RT–PCR machine with primers that corresponded to residues conserved in both the FSS13025 and Brazil Fortaleza genomes (GenBank numbers: KU955593.1, KX811222.1)[49]. To adhere to stringent guidelines, cycle threshold values >38 were deemed to indicate that RNA was not reliably detected and were not reported. Copy number sensitivity, as determined using a standard curve from diluted known quantities of ZIKV genome, was 25 copies per qPCR reaction.

ZIKV isolation from maternal plasma. Confluent T75 flasks of C6/36 cells were incubated with 300 µl of dam plasma from CTRL 2, ZIKA 3, ZIKA 4 and ZIKA 5 in two stages: first, cells and plasma were incubated with 6.5 ml complete DMEM (cDMEM) for 2 h at 28 °C; second, an additional 4 ml of cDMEM was added to each flask and incubated at 28 °C for 2 d. Two days post-inoculation (d.p.i.), growth medium was replaced and cells were incubated for an additional 7 d prior to harvest of culture fluid; at this time (9 d.p.i.), culture fluid was harvested and centrifuged at 1,260*g* for 10 min (4 °C) to clear cell debris. Aliquots were stored at −80 °C.

Immunofluorescence detection of ZIKV in Vero cells. Vero cells seeded onto coverslips were inoculated with 150 µl of culture fluid derived from ZIKV-infected nonhuman primate plasma at 9 d.p.i. and then incubated at 37 °C for 2 h with gentle rocking. Subsequently, medium was replaced, and infected cells were incubated for 22 h to allow virus growth and then fixed for 30 min with 4% (wt/vol) paraformaldehyde in TBS. Fixed cells were washed with TBS and permeabilized for 10 min at −20 °C with methanol. Cells were blocked with 5% (vol/vol) normal goat serum in TBS (NGS–TBS) and were stained with ZV-13 mouse monoclonal antibody reactive to ZIKV E protein (provided by M. Diamond, Washington University) in NGS–TBS[50]. Cells were subsequently incubated with goat anti–mouse IgG–Alexa Fluor 488 conjugate (cat no. A-11029, Thermo Fisher Scientific, MA) in NGS–TBS. Nuclei were counterstained with DAPI (cat no. D1306, Thermo Fisher Scientific) and coverslips were mounted on slides for analysis. Confocal immunofluorescent images were acquired using a Nikon Eclipse Ti microscope and analyzed using NIS-Elements imaging system software (version 4.51) (Nikon Instruments).

Immunofluorescence detection of TBR2, SOX2 and DCX in dentate gyrus of fetal hippocampus. Blinded and coded FFPE 5-µm sections were deparaffinized, and antigen was retrieved through incubating slides in 10 mM sodium citrate, pH 6.0, at 95 °C in a water bath for 35 min; slides were then cooled to room temperature and transferred to 1× PBS with 0.3% Triton X-100 (PBT). Sections were blocked (PBT with 5% donkey serum and 5% BSA) for 1 h and incubated with SOX2, TBR2 and DCX primary antibodies overnight at room temperature. Sections were washed three times with PBT, and species-specific Alexa Fluor 488 (donkey anti-mouse, cat no. A-21202, Thermo Fisher Scientific, MA), 568 (donkey anti-mouse, cat no. A-21202, Thermo Fisher Scientific, MA) and 647 (donkey anti-goat, cat no. A-21447, Thermo Fisher Scientific, MA) fluorescent secondary antibodies were applied (1:500). Sections were incubated for 2 h at room temperature, washed, counterstained with DAPI and mounted in Fluoromount-G. Confocal microscopic (20×) image volumes were acquired using a Zeiss 710 34-Quasar LSCM from the same four representative regions across the length of each dentate gyrus. Blinded and coded image volumes were visualized and analyzed using Imaris (Bitplane). Snapshots of overlaid and individual image volumes were exported and assembled using Adobe Photoshop and Illustrator.

Flow cytometry on placental tissues, maternal blood and fetal brain. To generate single-cell suspensions, chorioamniotic membranes were washed twice in sterile PBS, weighed and resuspended in digestion buffer (10 ml/g tissue; 20 mM HEPES, 30 mM $NaHCO_3$, 10 mg/ml BSA, 150 µg/ml DNase, 1 mg/ml bovine testes hyaluronidase, 200 U/ml collagenase 1a, 100 U/ml penicillin and 100 µg/ml streptomycin). The membranes were minced for 2 min and incubated at 37 °C at 300 r.p.m. for 1 h. Tissues were progressively filtered through a 280-µm metal sieve and then 100-, 70- and 40-µm nylon screens. Single cells were pelleted at 300*g* for 5 min and resuspended in RPMI supplemented with 10% heat-inactivated FBS, 100 U/ml penicillin, 100 µg/ml streptomycin and placed on ice. Erythrocyte lysis was performed on placental

and maternal blood single-cell suspensions by resuspending cells in erythrocyte lysing solution (lysis solution volume equal to 10 volumes of the cell pellet; 0.15 nM NH_4Cl, 1 mM $NaHCO_3$) followed by incubation for 15 min at room temperature. This process was repeated 3–5 times until erythrocytes were visibly absent. To generate single-cell suspensions of white matter and hippocampal tissues, each sample was filtered through a 280-μm metal sieve, pelleted at 300g for 5 min, washed once in sterile PBS and resuspended in FACS buffer (1 mM EDTA, 25 mM HEPES and 0.1% BSA (wt/vol) in PBS). Single-cell suspensions from all tissues were counted using the TC20 cell counter (Bio-Rad) and were diluted to approximately 10^7 cells/ml in FACS buffer. Cell suspensions from the fetal hippocampus were stored in formalin at 4 °C or 3.7% paraformaldehyde (1:2) or −80 °C, until samples from each monkey were collected[51].

Extracellular staining. Prior to staining, cells from all tissues were pretreated with Fc block (1:200, BD Biosciences) for 15 min. Cell suspensions from white matter tissue were stained with anti-CD56 V450 for 35 min (**Supplementary Table 5**), and cells from the placental membranes and maternal blood were stained with anti-CD3-FITC, anti-CD8-PerCP/Cy5.5 and anti-CD16-PE/Cy7 for 35 min (**Supplementary Table 5**). Cells were washed twice in FACS buffer to remove excess antibody.

Intracellular staining. Cells from white matter tissue were treated with the FOXP3 Transcription Factor Staining Buffer Set (eBioscience) per the manufacturer's instructions. Cells were stained with anti-GFAP-APC for 35 min (**Supplementary Table 5**) and then washed twice in permeabilization buffer (eBioscience) and resuspended in FACS buffer. At the time of analysis, hippocampal cells were washed twice with FACS buffer to remove residual fixative and permeabilized in 1× PBS, 0.1% Triton X-100 (Sigma-Aldrich, MO) and 1% BSA for 10 min on ice. Following permeabilization, cells were split into equal volumes and washed twice in FACS buffer. Hippocampal cells were treated with anti-TBR2-PE for 35 min (**Supplementary Table 5**) and then washed twice in FACS buffer to remove excess antibody.

Flow cytometry analysis. All stained cells were analyzed using an LSRII flow cytometer (BD Biosciences). Unstained and single-color compensation beads (BD Biosciences) were included for compensation. Cell surface and intracellular markers were analyzed using FlowJo software version 10.1 (FlowJo).

Flow cytometry on blood for antibody-dependent enhancement experiments. Peripheral blood from two healthy, flavivirus-naive adult pigtail macaques (CTRL I and J; **Supplementary Table 1**) were used to obtain peripheral blood mononuclear cells (PBMCs), which were enriched using density gradient centrifugation with Ficoll-Paque PLUS (GE Healthcare). Erythrocytes were lysed with ACK Lysis buffer (Gibco). Total PBMCs were resuspended in serum-free infection medium (RPMI 1640 medium plus 0.1 mM nonessential amino acids, 100 U/ml penicillin, 100 mg/ml streptomycin, 2 mM GlutaMAX, 10 mM HEPES (Cellgro) and 2-mercaptoethanol). The EDE2 B7 monoclonal antibody was synthesized by Lake Pharma (Belmont, CA). ZIKV PRVABC59 was originally obtained from the Centers of Disease Control and Prevention (Atlanta, GA), and 800 μl of ZIKV-infected C6/36 cell culture supernatant was used per well in this assay. Uninfected C6/36 cell culture supernatant ('spent medium', 800 μl) was used for wells not treated with ZIKV. Treatment conditions included: (i) no antibody and no virus, (ii) no antibody plus ZIKV, (iii) 5 μg/ml isotype antibody control (BioXcell) plus ZIKV or (iv) 1 μg/ml EDE2 B7 antibody plus ZIKV. All conditions were assayed in duplicate on 12-well plates (Corning). Virus and antibodies were first added to appropriate wells, mixed and then incubated at 37 °C and 5% CO_2 for 1 h, after which

2×10^6 PBMCs were added per well. After 2 h of incubation, 1 ml of 10% inactivated FBS (Gibco) infection medium was added to each well, and cultures were collected after 20 h. Adherent cells were treated with 5 mM cold EDTA at 4 °C for 30 min to assist with cell detachment and were gently removed using soft rubber-tipped scrapers (Falcon). Detached cell fractions were combined with suspension cultures, washed with Flow Cytometry Staining Buffer (eBioscience/Thermo Fisher Scientific) and stained with antibodies targeting surface markers CD14 (clone M5E2; BD Biosciences) and HLA-DR (clone G46-6; BD Biosciences) in the presence of Fixable LIVE/DEAD Discriminator (Invitrogen). Cells were fixed and permeabilized using Intracellular Fixation and Permeabilization Buffers (eBioscience/Thermo Fisher Scientific) according to the manufacturer's instructions. Intracellular staining with 4G2 antibody conjugated to Alexa Fluor 488 (Molecular Probes) was used to detect ZIKV antigen. Cells were fixed in 1% formalin, transferred to staining buffer and acquired on an LSRII cytometer (BD). Cells were first gated to exclude debris, omit doublet events and remove dead cells from analysis. $CD14^+HLA-DR^+$ double-positive events ('monocytes') were analyzed for the presence of ZIKV antigen. Cytometric data were analyzed using FlowJo X software (TreeStar).

Statistical analysis. An unpaired two-tailed Welch's t-test with unequal variances was used for all statistical analyses, and $P < 0.05$ was considered significant. Statistical analysis was performed using GraphPad Prism (version 6.0, GraphPad Software, USA; http://www.graphpad.com/) and Stata (version 14.2, StataCorp, TX, USA). The fetal brain volume ratio analysis excluded ZIKA 4 because final MRI data were obtained ~30 d earlier in this case than for all other cases and controls.

Life Sciences Reporting Summary. Further information on experimental design is available in the **Life Sciences Reporting Summary**.

Data availability. No large datasets were generated or analyzed during the current study. All data analyzed in this study are included in this published article (and its supplementary information files).

41. Styer, L.M. et al. Mosquitoes inoculate high doses of West Nile virus as they probe and feed on live hosts. PLoS Pathog. **3**, 1262–1270 (2007).
42. Woods, S.E., Marini, R.P. & Patterson, M.M. Noninvasive temporal artery thermometry as an alternative to rectal thermometry in research macaques (Macaca spp.). J. Am. Assoc. Lab. Anim. Sci. **52**, 295–300 (2013).
43. Price, D.P. et al. The fat body transcriptomes of the yellow fever mosquito Aedes aegypti, pre- and post- blood meal. PLoS One **6**, e22573 (2011).
44. Conrad, S. et al. Ultrasound measurement of fetal growth in Macaca nemestrina. Am. J. Primatol. **36**, 15–35 (1995).
45. Kim, K. et al. Intersection based motion correction of multislice MRI for 3-D in utero fetal brain image formation. IEEE Trans. Med. Imaging **29**, 146–158 (2010).
46. Kim, K. et al. Bias field inconsistency correction of motion-scattered multislice MRI for improved 3D image reconstruction. IEEE Trans. Med. Imaging **30**, 1704–1712 (2011).
47. Fogtmann, M. et al. A unified approach to diffusion direction sensitive slice registration and 3-D DTI reconstruction from moving fetal brain anatomy. IEEE Trans. Med. Imaging **33**, 272–289 (2014).
48. Habas, P.A. et al. A spatiotemporal atlas of MR intensity, tissue probability and shape of the fetal brain with application to segmentation. Neuroimage **53**, 460–470 (2010).
49. Lanciotti, R.S. et al. Genetic and serologic properties of Zika virus associated with an epidemic, Yap State, Micronesia, 2007. Emerg. Infect. Dis. **14**, 1232–1239 (2008).
50. Zhao, H. et al. Structural basis of Zika virus–specific antibody protection. Cell **166**, 1016–1027 (2016).
51. Thomsen, E.R. et al. Fixed single-cell transcriptomic characterization of human radial glial diversity. Nat. Methods **13**, 87–93 (2016).